Wind and Structures, *Vol. 16, No. 6 (2013) 561-577*
DOI:http://dx.doi.org/10.12989/was.2013.16.6.561

Extraction of rational functions by forced vibration method for time-domain analysis of long-span bridges

Bochao Cao[1,2] and Partha P. Sarkar[*1]

[1]2271 Howe Hall, Department of Aerospace Engineering, Iowa State University, Ames, IA, 50011-2271, USA
[2]Department of Mechanics and Engineering Science, Fudan University, PR China

(Received September 12, 2011. Revised June 21, 2012, Accepted July 7, 2012)

Abstract. Rational Functions are used to express the self-excited aerodynamic forces acting on a flexible structure for use in time-domain flutter analysis. The Rational Function Approximation (RFA) approach involves obtaining of these Rational Functions from the frequency-dependent flutter derivatives by using an approximation. In the past, an algorithm was developed to directly extract these Rational Functions from wind tunnel section model tests in free vibration. In this paper, an algorithm is presented for direct extraction of these Rational Functions from section model tests in forced vibration. The motivation for using forced-vibration method came from the potential use of these Rational Functions to predict aerodynamic loads and response of flexible structures at high wind speeds and in turbulent wind environment. Numerical tests were performed to verify the robustness and performance of the algorithm under different noise levels that are expected in wind tunnel data. Wind tunnel tests in one degree-of-freedom (vertical/torsional) forced vibration were performed on a streamlined bridge deck section model whose Rational Functions were compared with those obtained by free vibration for the same model.

Keywords: flutter analysis; time-domain method; rational function approximation; forced vibration; long-span bridges

1. Introduction

Analysis to predict wind-induced flutter instability of flexible structures is usually conducted in frequency domain, since the self-excited aerodynamic forces induced by motion of structures are expressed by the well-known flutter derivatives (Scanlan and Tomko 1971) that are functions of reduced frequency. Flutter derivatives can be identified at discrete reduced frequencies (or reduced velocities) through either free vibration (Chowdhury and Sarkar 2003, Chen *et al*. 2008, Chen and Kareem 2008, Bartoli *et al*. 2009, Ding *et al*. 2010) or forced vibration (Matsumoto 1996, Haan 2000) method using section models in wind tunnels. However, when dealing with wind interacting with nonlinear structures or structures excited by non-stationary winds, the time-domain method (Lin and Ariaratnam 1980, Scanlan 1993, Chen and Kareem 2002, Caracoglia and Jones 2003, Zhang *et al*. 2011) is more suitable and preferable. Roger (1977) developed a Rational Function Approximation (RFA) using least squares (LS) method for approximation of self-excited forces

∗Corresponding author, Professor, E-mail: ppsarkar@iastate.edu

http://www.techno-press.org/?journal=was&subpage=8 ISSN: 1226-6116 (Print), 1598-6225 (Online)

with rational functions in Laplace domain that can be used in time-domain analysis. These functions can be indirectly extracted from experimentally obtained flutter derivatives using approximation techniques. Karpel (1982) developed another RFA formulation using minimum state method known as MS-RFA that involves lesser computational work while maintaining higher accuracy of approximation compared to LS-RFA by Roger. RFA formulation has been applied to bridge aerodynamics by several researchers including Chen *et al*. (2000). To accelerate the process of extraction of Rational Functions, Chowdhury and Sarkar (2005) developed a method through which Rational Functions can be extracted directly from free vibration experiments in a wind tunnel at fewer wind velocities compared to those used for extracting flutter derivatives. It is known that the free vibration method has some limitations compared to the forced vibration method, particularly, at higher wind velocities and for turbulent flow. This provides the motivation of developing a forced vibration method to extract the Rational Functions from wind tunnel tests.

In this paper, a new algorithm for forced vibration experimental method that was developed for direct extraction of Rational Functions is presented. Results from both numerical simulation and wind tunnel tests are presented to validate the algorithm. A streamlined bridge deck section model with a chord-to-thickness ratio of about 15:1 was used as an example.

2. Formulation and algorithm

In two degree-of-freedom (DOF), self-excited forces acting on the structure can be calculated from flutter derivative formulation as given below

$$L_{se}(t) = \frac{1}{2}\rho U^2 B\left[\mathrm{K}H_1^*(K)\frac{\dot{h}}{U} + \mathrm{K}H_2^*(K)\frac{B\dot{\alpha}}{U} + \mathrm{K}^2 H_3^*(K)\alpha + \mathrm{K}^2 H_4^*(K)\frac{h}{B}\right] \tag{1}$$

$$M_{se}(t) = \frac{1}{2}\rho U^2 B^2\left[\mathrm{K}A_1^*(K)\frac{\dot{h}}{U} + \mathrm{K}A_2^*(K)\frac{B\dot{\alpha}}{U} + \mathrm{K}^2 A_3^*(K)\alpha + \mathrm{K}^2 A_4^*(K)\frac{h}{B}\right] \tag{2}$$

where L_{se} = self-excited lift, M_{se} = self-excited torsional moment, ρ = air density, U = mean wind speed, B = width of bridge deck model, $K = B\omega/U$ = reduced frequency, where $\omega = 2\pi f$ = circular frequency of the vibration, $h(t, x)$ = vertical displacement, $\alpha(t, x)$ = torsional displacement, $(\dot{\ })$ = $d(\ )/dt$, H_i^*, A_i^* (i=1,…,4) = flutter derivatives which are aeroelastic coefficients changing with reduced frequency.

Applying Laplace transformation on Eqs. (1) and (2)

$$\begin{bmatrix}\hat{L}_{se}\\ \hat{M}_{se}\end{bmatrix} = \underline{V}_f\underline{\tilde{Q}\hat{q}} = \begin{bmatrix}\frac{1}{2}\rho U^2 B & 0\\ 0 & \frac{1}{2}\rho U^2 B^2\end{bmatrix}\begin{bmatrix}\mathrm{K}^2 H_4^*(K) + p.\mathrm{K}H_1^*(K) & \mathrm{K}^2 H_3^*(K) + p.\mathrm{K}H_2^*(K)\\ \mathrm{K}^2 A_4^*(K) + p.\mathrm{K}A_1^*(K) & \mathrm{K}^2 A_3^*(K) + p.\mathrm{K}A_2^*(K)\end{bmatrix}\begin{bmatrix}\hat{h}/B\\ \hat{\alpha}\end{bmatrix} \tag{3}$$

where $p = iK$ = non-dimensional Laplace domain variable, and '^' denotes the Laplace transformation of the corresponding time domain function. By Karpel (1982)'s minimum state

RFA formulation with neglect of second order term, the matrix $\underline{\tilde{Q}}$ can be approximated by $\underline{Q}$, which is a matrix of rational functions in Laplace domain, as given below

$$\underline{Q}(p) = \underline{A}_0 + \underline{A}_1 p + \underline{D}\left(p\underline{I} + \underline{R}\right)^{-1} \underline{E}p \tag{4}$$

where $\underline{A}_0$, $\underline{A}_1$ are stiffness matrix and damping matrix, respectively, $\underline{D}$ and $\underline{E}$ are lag matrices, $\underline{R}$ is a diagonal matrix with diagonal elements of lag coefficients, and the dimension of the matrix $\underline{R}$ is the number of lag terms. Since Chowdhury and Sarkar (2005) showed that the formulation with even one lag term works well for streamlined and bluff bridge decks, only formulation with one lag term is used here. With only one lag term, Eq. (4) can be written as given below

$$\underline{Q}(p) = \begin{bmatrix} \underline{Q}_{11} & \underline{Q}_{12} \\ \underline{Q}_{21} & \underline{Q}_{22} \end{bmatrix} = \underline{A}_0 + \underline{A}_1 p + \begin{bmatrix} \underline{D}_{11} \\ \underline{D}_{21} \end{bmatrix} \frac{p}{p+\lambda} \begin{bmatrix} \underline{E}_{11} & \underline{E}_{12} \end{bmatrix} = \underline{A}_0 + \underline{A}_1 p + \frac{p}{p+\lambda} \begin{bmatrix} \underline{F}_{11} & \underline{F}_{12} \\ \underline{F}_{21} & \underline{F}_{22} \end{bmatrix} = \underline{A}_0 + \underline{A}_1 p + \frac{p}{p+\lambda} \underline{F} \tag{5}$$

where $\underline{A}_0, \underline{A}_1, \underline{F}$ and λ are referred here as Rational Function Coefficients.

Substituting Eq. (5) into Eq. (3), self-excited aerodynamic forces in Laplace domain can be obtained

$$\hat{L}_{se} = \frac{1}{2}\rho U^2 B \left[\left((\underline{A}_0)_{11} + (\underline{A}_1)_{11} p + \frac{\underline{F}_{11} p}{p+\lambda} \right) \quad \left((\underline{A}_0)_{12} + (\underline{A}_1)_{12} p + \frac{\underline{F}_{12} p}{p+\lambda} \right) \right] \underline{\hat{q}} \tag{6}$$

$$\hat{M}_{se} = \frac{1}{2}\rho U^2 B^2 \left[\left((\underline{A}_0)_{21} + (\underline{A}_1)_{21} p + \frac{\underline{F}_{21} p}{p+\lambda} \right) \quad \left((\underline{A}_0)_{22} + (\underline{A}_1)_{22} p + \frac{\underline{F}_{22} p}{p+\lambda} \right) \right] \underline{\hat{q}} \tag{7}$$

To obtain higher accuracy, formulation with two lag terms could be used, as derived in Chowdhury (2004).

Applying inverse Laplace transformation on Eqs. (6) and (7), time domain formulations can be obtained as given below

$$\dot{L}_{se} + \lambda \frac{U}{B} L_{se} = \frac{1}{2}\rho U^2 B \left(\left(\frac{U}{B} \right) \underline{\psi}_1 \underline{q} + \underline{\psi}_2 \underline{\dot{q}} + \left(\frac{B}{U} \right) \underline{\psi}_3 \underline{\ddot{q}} \right) \tag{8}$$

$$\dot{M}_{se} + \lambda \frac{U}{B} M_{se} = \frac{1}{2}\rho U^2 B^2 \left(\left(\frac{U}{B} \right) \underline{\psi}_4 \underline{q} + \underline{\psi}_5 \underline{\dot{q}} + \left(\frac{B}{U} \right) \underline{\psi}_6 \underline{\ddot{q}} \right) \tag{9}$$

where $\underline{\psi}_1 = \left[\lambda\left(\underline{A}_0\right)_{11} \quad \lambda\left(\underline{A}_0\right)_{12}\right]$, $\underline{\psi}_2 = \left[\left(\underline{A}_0\right)_{11} + \lambda\left(\underline{A}_1\right)_{11} + \underline{F}_{11} \quad \left(\underline{A}_0\right)_{12} + \lambda\left(\underline{A}_1\right)_{12} + \underline{F}_{12}\right]$,
$\underline{\psi}_3 = \left[\left(\underline{A}_1\right)_{11} \quad \left(\underline{A}_1\right)_{12}\right]$, $\underline{\psi}_4 = \left[\lambda\left(\underline{A}_0\right)_{21} \quad \lambda\left(\underline{A}_0\right)_{22}\right]$,
$\underline{\psi}_5 = \left[\left(\underline{A}_0\right)_{21} + \lambda\left(\underline{A}_1\right)_{21} + \underline{F}_{21} \quad \left(\underline{A}_0\right)_{22} + \lambda\left(\underline{A}_1\right)_{22} + \underline{F}_{22}\right]$, $\underline{\psi}_6 = \left[\left(\underline{A}_1\right)_{21} \quad \left(\underline{A}_1\right)_{22}\right]$

In a forced vibration method, the model is constrained to vibrate in one-DOF, vertical, torsional or horizontal motion, where the displacement is a sinusoidal motion at a prescribed amplitude and frequency. For the current study, experiments in vertical and torsional degrees of freedom were performed to validate the new method, respectively.

In vertical motion experiment, the displacements h and α can be written as

$$h = h_0 \cos\left(\omega_h t\right), \quad \alpha = 0 \tag{10}$$

At a certain mean wind velocity, U_1, since there is a lag between self-excited aerodynamic loads (lift and moment) and the corresponding displacement, the self-excited loads can be written as

$$L_{se} = L_{h0}^{1} \cos\left(\omega_h t - \phi_{Lh}^{1}\right) \tag{11}$$

$$M_{se} = M_{h0}^{1} \cos\left(\omega_h t - \phi_{Mh}^{1}\right) \tag{12}$$

Substituting Eqs. (10) and (11) into Eq. (8)

$$\begin{aligned} &-L_{h0}^{1}\omega_h \sin(\omega_h t - \phi_{Lh}^{1}) + \lambda \frac{U_1}{B} L_{h0}^{1} \cos(\omega_h t - \phi_{Lh}^{1}) \\ &= \frac{1}{2}\rho U_1^{\,2} B\left(\left(\frac{U_1}{B}\right)\left(\underline{\psi}_1\right)_1 \frac{h_0 \cos(\omega_h t)}{B} - \left(\underline{\psi}_2\right)_1 \frac{h_0 \omega_h \sin(\omega_h t)}{B} - \left(\frac{B}{U_1}\right)\left(\underline{\psi}_3\right)_1 \frac{h_0\left(\omega_h\right)^2 \cos(\omega_h t)}{B}\right) \end{aligned} \tag{13}$$

By matching coefficients of $\sin(\omega_h t)$ and $\cos(\omega_h t)$ above, following equations can be obtained

$$\begin{aligned} &\left[\omega_h B \sin\phi_{Lh}^{1} + \lambda U_1 \cos\phi_{Lh}^{1}\right]\frac{L_{h0}^{1}}{h_0} = \frac{1}{2}\rho\left(U_1\right)^2 B\left(\left(\frac{U_1}{B}\right)\left(\underline{\psi}_1\right)_1 - \left(\frac{B}{U_1}\right)\left(\underline{\psi}_3\right)_1\left(\omega_h\right)^2\right) \\ &\left[\omega_h B \cos\phi_{Lh}^{1} - \lambda U_1 \sin\phi_{Lh}^{1}\right]\frac{L_{h0}^{1}}{h_0} = \frac{1}{2}\rho\left(U_1\right)^2 B\left(\underline{\psi}_2\right)_1 \omega_h \end{aligned} \tag{14a}$$

Eq. (14(a)) can be re-written in matrix form

$$\begin{bmatrix} \frac{1}{2}\rho(U_1)^3 & 0 & -\frac{1}{2}\rho U_1 B^2(\omega_h)^2 & -U_1\frac{L_{h0}^1}{h_0}\cos\phi_{Lh}^1 \\ 0 & \frac{1}{2}\rho(U_1)^2 B\omega_h & 0 & U_1\frac{L_{h0}^1}{h_0}\sin\phi_{Lh}^1 \end{bmatrix}\begin{bmatrix} (\underline{\psi_1})_1 \\ (\underline{\psi_2})_1 \\ (\underline{\psi_3})_1 \\ \lambda \end{bmatrix} = \omega_h\frac{B}{h_0}\begin{bmatrix} L_{h0}^1\sin\phi_{Lh}^1 \\ L_{h0}^1\cos\phi_{Lh}^1 \end{bmatrix} \quad (14b)$$

Since the above equations have four unknowns, $(\underline{\psi_1})_1$ to $(\underline{\psi_3})_1$ and λ, it cannot be solved. However, if similar equations are written for two more wind velocities, U_2 and U_3, and combined with Eq. (14(b)) , the following matrix of six equations in terms of the four unknowns can be obtained

$$\underline{C_{h1}}\,\underline{X_{h1}} = \underline{D_{h1}} \quad (15)$$

where $\underline{C_{h1}}$, $\underline{X_{h1}}$, $\underline{D_{h1}}$ are defined in Appendix A (Eqns. A.1-A.3).

By Least Squares method, the unknown vector $\underline{X_{h1}}$ can be solved as

$$\underline{X_{h1}} = \left[\underline{C_{h1}}^T\underline{C_{h1}}\right]_{4\times4}^{-1}\left[\underline{C_{h1}}^T\underline{D_{h1}}\right]_{4\times1} \quad (16a)$$

Similarly, by substituting Eqs. (10) and (12) into Eq. (9), the unknown vector $\underline{X_{h2}}$ can be solved as

$$\underline{X_{h2}} = \left[\underline{C_{h2}}^T\underline{C_{h2}}\right]_{4\times4}^{-1}\left[\underline{C_{h2}}^T\underline{D_{h2}}\right]_{4\times1} \quad (16b)$$

where $\underline{C_{h2}}$, $\underline{X_{h2}}$, $\underline{D_{h2}}$ are defined in Appendix A (Eqns. A.4-A.6).

In this algorithm, data from experiments at only three wind speeds (U_1 to U_3) are needed which is the minimum requirement for the least squares method. However, to increase the accuracy of the algorithm, data collected at more number of wind speeds could be included. This will add more number of rows in the matrix $\underline{C_{hi}}$ and vector $\underline{D_{hi}}$.

Finally, from vectors $\underline{X_{h1}}$ and $\underline{X_{h2}}$, $(\underline{A_0})_{11}, (\underline{A_0})_{21}, (\underline{A_1})_{11}, (\underline{A_1})_{21}, (\underline{F})_{11}, (\underline{F})_{21}$ and λ can be obtained, and Q_{11} and Q_{21} can be obtained from Eq. (5). Following a similar procedure, using data from forced vibration experiments under torsional motion of the model $(\underline{A_0})_{12}, (\underline{A_0})_{22}, (\underline{A_1})_{12}, (\underline{A_1})_{22}, (\underline{F})_{12}, (\underline{F})_{22}$ and λ, as well as Q_{12} and Q_{22}, can be obtained. It is noted that λ for the vertical motion case and torsional motion case may not be the same.

Thus, this algorithm will require simultaneous measurements of the displacements (h or α) along with the surface pressures on the model that will help compute the self-excited forces, lift (L_{se}) and moment (M_{se}). Amplitudes of the self-excited forces (L_{se} and M_{se}) that are computed from pressures and their phase lags (ϕ's) with respect to displacement (h or α) along with amplitude and frequency of the displacement and the mean wind speeds are used as input to the algorithm.

3. Experimental set-up

3.1 Wind tunnel used

The experiments were performed in the Bill James Open-Return Wind Tunnel, which is located in the Wind Simulation and Testing Laboratory (WiST Lab) in the Department of Aerospace Engineering at Iowa State University. This wind tunnel has a test section of 0.915 m (3.0ft) width by 0.762 m (2.5ft) height and its maximum wind velocity is 75 m/s (246 ft/s).

3.2 Model, suspension system and forced vibration mechanism

A streamlined bridge deck section model was used in the experiment as shown in Figs. 1 and 2.

The model is composed of a shallow box girder section and two semi-circular fairings at the edges. The length, chord length and thickness of the model are about 0.533 m, 0.3 m, and 0.02 m, respectively. The three-DOF model suspension system and two Plexiglas end plates that were used to reduce the edge defects on the model are shown in Fig. 2. This system was developed by Sarkar *et al*. (2004). The suspension system enables vertical, horizontal and torsional motions of the model. In the current experiments, sinusoidal vertical and torsional motions of the model with constant amplitudes and frequencies are realized by the driving mechanism connected to the model suspension system with four aluminum rods as shown in Fig. 2. The entire mechanism is driven by two motors which are placed above the test section, as seen in Fig. 3. By changing the rotating speed of two motors using two separate controllers, the two frequencies of model vibration in two degrees of freedom can be changed independently.

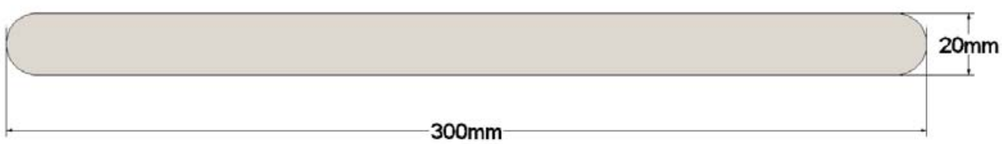

Fig.1 Cross section of the streamlined bridge deck model used in the experiment

3.3 Displacement measurement

The vertical displacement of the model was measured by measuring the spring force in each of two springs which is connected to the model at one end and a strain gage force transducer at the other end. The torsional displacement was measured by measuring the torque at one end of the model shaft using a torque transducer which is mounted on the suspension system. LabView was used for data acquisition, where the sampling rate was set at 625 Hz.

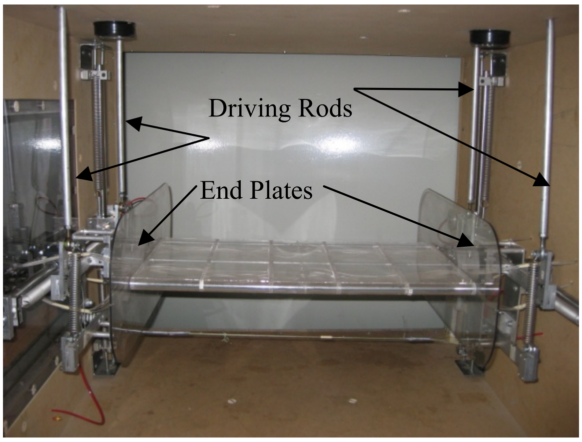

Fig. 2 Bridge deck model and suspension system

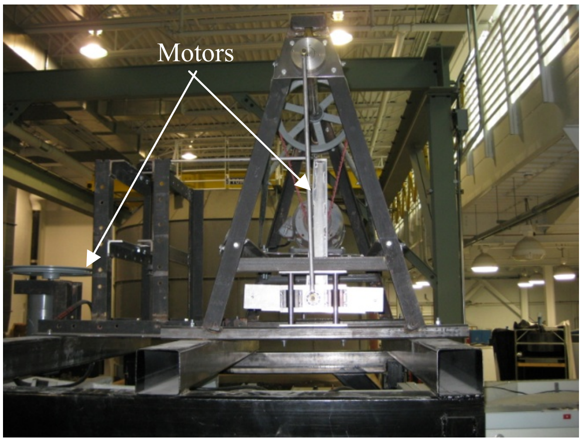

Fig. 3 Driving mechanism

3.4 Aerodynamic force measurement

The algorithm stated in this paper, in addition to the displacement time histories, requires the time histories of aerodynamic forces acting on the model while it is vibrating. The aerodynamic forces were obtained from the measured surface pressures on the vibrating model through numerical integration (trapezoidal law). Surface pressures were measured on the model including the fairings through a row of pressure taps located on the upper and lower surfaces of the model along the mid-plane. In total, forty-two pressure taps were used in this test, equally distributed on both the surfaces. The pressure taps are denser on the upstream side than the downstream side of the model. Two 64-channel pressure modules (Scanivalve ZOC33/64 Px) were used to measure the pressure. The sampling rate for pressure measurement was 312.5 Hz (half of displacement sampling rate) in the experiment. To synchronize the pressure data with the displacement data, the pressure transducers were set to work in external-trigger mode. The LabView program that was used for displacement data acquisition was programmed to output a digital signal when the displacement data acquisition started, so that the pressure data acquisition system would receive this external signal and get triggered to start the acquisition of pressure. A separate program RAD (Scanivalve) was used to collect the pressure data. The sampling rate (1000000/64/n) for the RAD software is calculated based on the specified time-lag (n) in micro seconds between each of the 64 channels of the ZOC33/64 transducer and its maximum sampling frequency need not exceed 500 Hz. Thus, the sampling rate for pressure measurement can be any real number whereas the sampling rate for the displacement measurement has to be an integer because it is measured using the LabView program. To synchronize the times at which both pressure and displacement data are sampled, it was decided to use 625 Hz sampling frequency for displacement and 312.5 Hz or half of 625 Hz as sampling frequency for pressures.

4. Results and discussions

4.1 Numerical tests and results

To validate the algorithm as presented here, numerical tests were done before using it with wind tunnel data. Firstly, the displacement time history of the model was generated as a sinusoidal function with the same amplitude and frequency as those of the wind tunnel tests. Secondly, the first derivative of the displacement history was generated through central difference method. Using the flutter derivatives for the cross section mentioned here (Chowdhury and Sarkar 2003, 2004), the aerodynamic lift and moment time histories (L_{se} and M_{se}) were generated. Using the lift, moment and displacement time histories as input, rational function coefficients were extracted using the algorithm developed here. The relationship between rational function coefficients and flutter derivatives, as given below, were used to calculate the flutter derivatives for comparison with those used

$$H_1^* = imag(Q_{11})/\mathrm{K}^2,\ H_4^* = real(Q_{11})/\mathrm{K}^2,\ A_1^* = imag(Q_{21})/\mathrm{K}^2,\ A_4^* = real(Q_{21})/\mathrm{K}^2$$
$$H_2^* = imag(Q_{12})/K^2,\ H_3^* = real(Q_{12})/K^2,\ A_2^* = imag(Q_{22})/K^2,\ A_3^* = real(Q_{22})/K^2 \tag{17}$$

An excellent agreement between the two sets of flutter derivatives proved the feasibility of the algorithm for extraction of rational function coefficients.

However, in a wind tunnel experiment, the test data can be contaminated with noise. Therefore, to test the robustness of the algorithm, white noise time histories with a normal probability distribution were scaled and added to the displacement and force time histories that were generated, and then rational function coefficients were extracted from these noisy data using the algorithm. The noise time histories were generated independently, and therefore they were not correlated to aerodynamic force and model displacement time histories. The standard deviation of the noise time histories was chosen as 10% and 20% of the respective signal amplitudes. The flutter derivatives extracted using Eq. (17) from these noisy data were compared with those extracted from the original numerical data, and the percentage errors (root mean square) were calculated as shown in Table 1. In Table 1, it is seen that H_4*, A_4*, H_2* and A_2* are more sensitive to the noise in the data than the rest of the flutter derivatives. However, the errors in all eight flutter derivatives change marginally even with the doubling of noise amplitudes.

Table 1 Percentage errors for derivatives drawn from noisy data

Noise Amplitudes	H_1*	H_4*	A_1*	A_4*	H_2*	H_3*	A_2*	A_3*
10%	0.3	5.0	0.2	1.8	0.9	0.2	1.1	1.0
20%	0.4	6.2	0.3	3.6	2.1	0.3	1.8	1.0

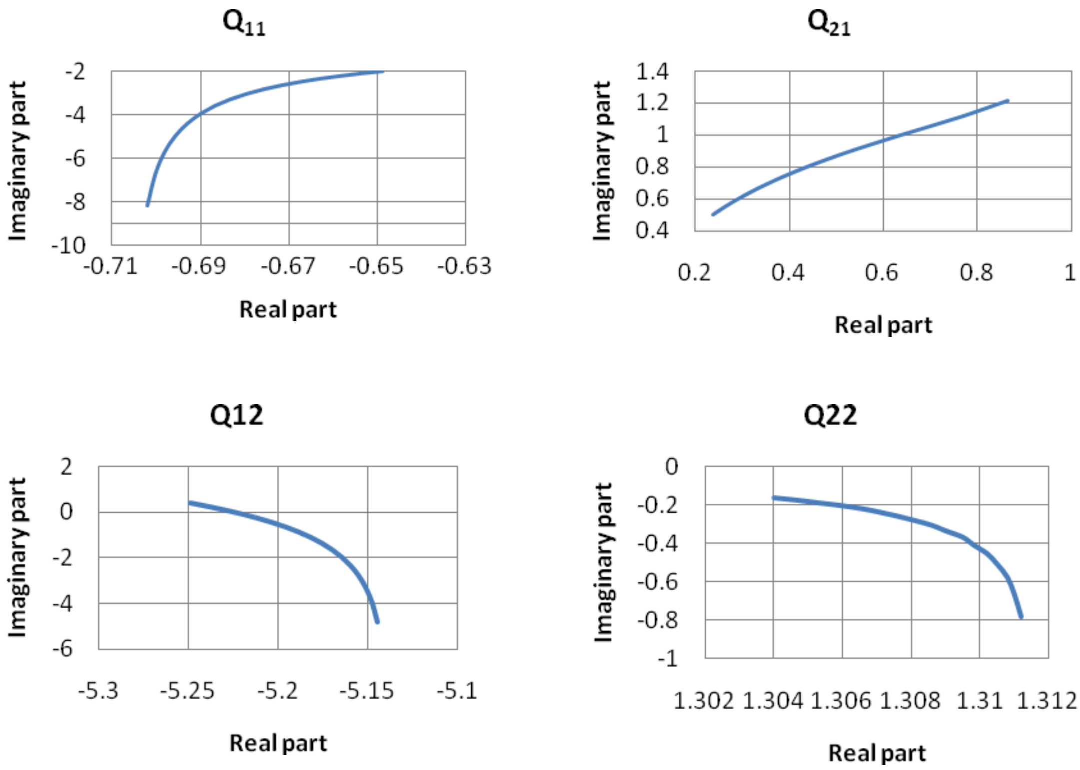

Fig. 4 Experimentally obtained rational functions

4.2 Experimental results

For vertical DOF forced vibration of the bridge deck model, wind tunnel tests were performed at wind speeds of 4 m/s, 6.7 m/s and 11.1 m/s, while for torsional DOF forced vibration, measurements were carried out at wind speeds of 3.6 m/s, 10.2 m/s and 15.2 m/s. The model was forced to vibrate at 2.44 Hz for vertical motion and 3.28 Hz for torsional motion. The rational functions Q_{11}, Q_{21}, Q_{12} and Q_{22} , as obtained by the algorithm and method mentioned here, are shown in Fig. 4. For the purpose of validation of the rational functions obtained using the proposed algorithm, these were converted to corresponding flutter derivatives of the streamlined bridge section and compared with those obtained earlier by free vibration method (Chowdhury and Sarkar 2003). However, error envelopes need to be assessed for each of these two data sets before the comparison. All eight flutter derivatives (H_1* to H_4*, A_1* to A_4*) were calculated using the obtained rational functions (Eq. (17)) and error envelopes of these flutter derivatives were obtained using perturbed rational functions that were extracted using modified phase lag angles, $\phi_{Lh}, \phi_{Mh}, \phi_{La}$ and ϕ_{Ma}, with ±7% error added to their obtained values. Similarly, error envelopes for flutter derivative data sets that were obtained by free vibration method (Chowdhury and Sarkar 2003) were calculated by adding ±7% errors to the original phase lag angles, $\phi_{Lh}, \phi_{Mh}, \phi_{La}$ and ϕ_{Ma}, obtained from the numerically generated displacement and force time histories without noise as in Section 4.1. Both sets of flutter derivatives and their corresponding error envelopes are plotted for comparison in Fig. 5.

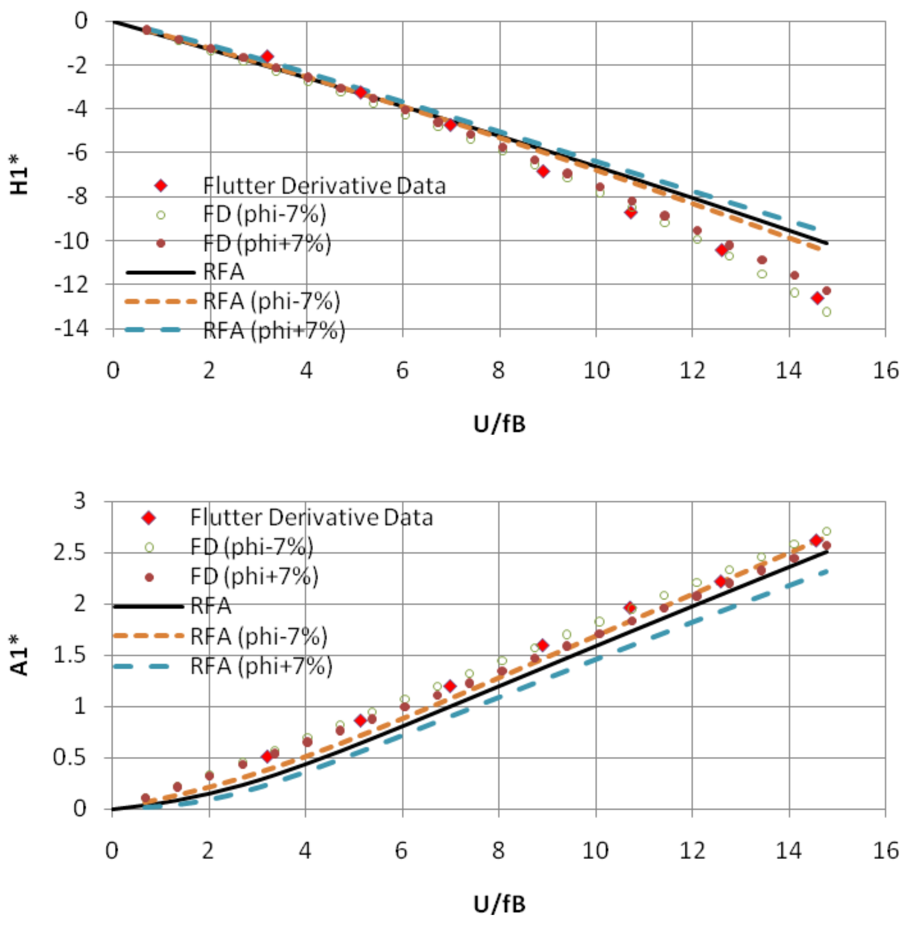

Continued

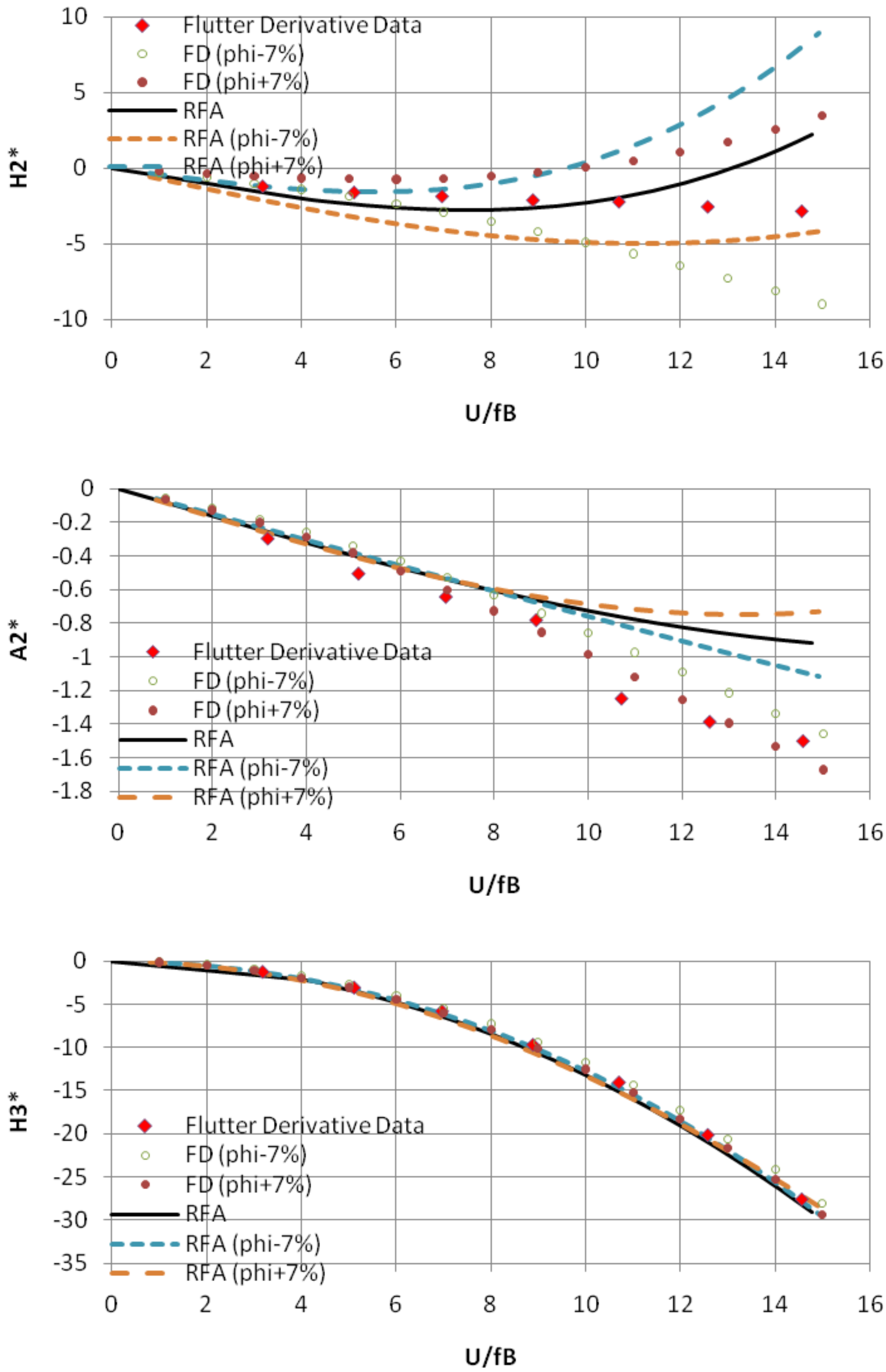

Flutter Derivative Data
FD (phi-7%)
FD (phi+7%)
RFA
RFA (phi-7%)
RFA (phi+7%)
H2*
A2*
H3*
U/fB

Continued

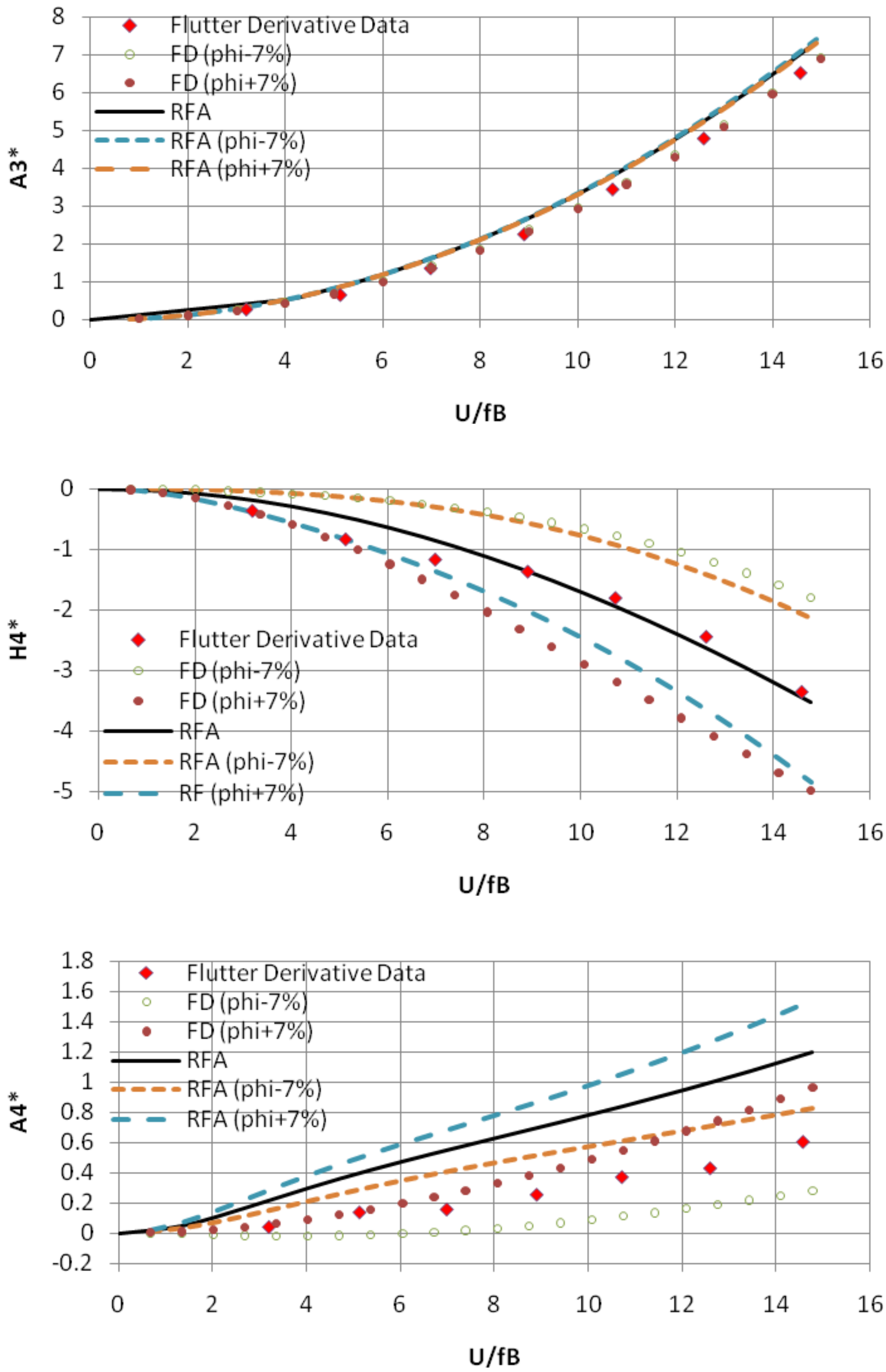

Fig. 5 Comparison of experimentally obtained flutter derivatives and those from experimental Rational Functions

These plot show that H_4*, A_1*, H_3* and A_3* match very well with earlier flutter derivative data obtained by free vibration method. H_1*, H_2* and A_2* curves match well for low reduced velocities and there are some differences at higher reduced velocities. This could be because the free vibration method need not be very accurate at high wind speeds when aerodynamic damping is positive and large. This difference could be also attributed to the fact that the free-vibration experiments were of two-DOF (vertical and torsional) while the forced vibration experiments stated here were two separate one-DOF motion experiments (vertical and torsional, respectively) for extraction of all eight flutter derivatives. It could be a combination of both reasons. The worst comparison is the A_4*curves. The A_4* extracted from RFA method here is almost twice of that free vibration method. This could be because of the difference in degrees of freedom or it could be because A_4* is more sensitive to the noise in the experimental data as concluded by numerical tests (Table 1). However, in Fig. 5, all the 7% error bands for flutter derives from RFA (rational function approximation) data overlap with corresponding 7% error bands for free vibration flutter derivative data. Moreover, from error bands plotted in Fig. 5, it is seen that H_4*, A_4* and H_2* are more sensitive to the phase difference than other flutter derivatives. This is similar to the results presented in Table 1. Actually, it has been shown by Sarkar *et al*. (2009) that, in forced vibration technique to extract flutter derivatives, slight error in estimation of the phase difference between aerodynamic loads and displacements obtained from experiments could get amplified in some of the flutter derivatives (A_2* and H_2* in Sarkar *et al*. 2009), which is similar to what is observed here in H_4*, A_4*, H_2* and A_2* plots in Fig. 5.

Table 2. Comparison of flutter speeds of the streamlined bridge deck section model obtained by different set of parameters

	Flutter Derivatives (Gan Chowdhury and Sarkar 2005) Free vibration	Rational Functions (Gan Chowdhury and Sarkar 2005) Free vibration	Rational Functions (Obtained in this paper) Forced vibration	Rational Functions (Obtained by adding ±2% error to flutter derivative data) Forced vibration
Flutter Speed, U_{cr} (m/s)	32.4	31.8	34.5	32.9 (-2%), 32.8 (+2%)

To further validate the method, the flutter speed of the streamlined bridge deck section model was predicted using time domain simulation and Rational Function Coefficients extracted here. For flutter speed prediction, the time domain equations of motion were solved, corresponding to a chosen wind speed, at each time step after substituting the Rational Function Coefficients that were extracted. This process is repeated for incremental wind speeds until a divergent response is obtained. The flutter speed obtained here was compared with that obtained by Gan Chowdhury and Sarkar (2005) for the same model using Rational Functions (free vibration) and flutter derivatives (free vibration) and shown in Table 2. In current research, the flutter speed of the model was not validated through free vibration wind tunnel experiment. To investigate the effect of error in phase difference on the prediction of flutter speed, the Rational Functions, obtained by adding ±2% errors to the exact value of $\phi_{Lh}, \phi_{Mh}, \phi_{La}$ and ϕ_{Ma}, calculated from the numerically generated displacement and aerodynamic load time histories using Gan Chowdhury and Sarkar's (2005) flutter derivative data, were also used to predict flutter speed of the bridge deck, and the results are listed in Table 2.

It can be seen from the table that the comparison of predicted flutter speed is good, though some of the flutter derivatives, especially A_4*, do not match very well with those extracted earlier, as shown in Fig. 5. Moreover, by ±2% error test, it is shown that slight error in phase difference, $\phi_{Lh}, \phi_{Mh}, \phi_{La}$ and ϕ_{Ma}, could lead to a change in predicted flutter speed.

Overall, this algorithm demonstrated the feasibility of direct extraction of rational functions by the forced vibration method.

5. Conclusions

In this paper, a new method has been introduced to directly extract rational function coefficients or rational functions from forced vibration experiment. Through numerical tests, it has been shown that the algorithm is feasible for extraction of rational function coefficients and it is quite robust. The validation results of the obtained rational functions show that flutter derivatives extracted from this RFA method are generally in good agreement with those from earlier free vibration experimental results, given their sensitivity to noise in the signals. Recently, all eight flutter derivatives were extracted simultaneously using a two-DOF forced-vibration system (Cao and Sarkar 2013) to eliminate the influence of single DOF (if any) on the final results. Moreover, to avoid the amplification of the error induced from phase difference identification in the algorithm as discussed previously, a new algorithm which is based on the system identification on the whole time histories rather than just the phase differences and amplitudes of time histories was developed and validated by wind tunnel tests (Cao and Sarkar 2013).

References

Bartoli, G., Contri, S., Mannini, C. and Righi, M. (2009), "Toward an improvement in the identification of bridge deck flutter derivatives", *J. Eng. Mech.- ASCE*, **135**(8), 771-785.

Cao, B. and Sarkar, P.P. (2013), "Identification of rational functions using two-degree-of-freedom model by forced vibration method", *Eng. Struct*., (in press).

Caracoglia, L. and Jones, N.P. (2003), "Time domain vs. frequency domain characterization of aeroelastic forces for bridge deck sections", J. *Wind Eng. Ind. Aerod*., **91**, 371-402

Chen, C., Wu, J. and Chen, J. (2008), "Prediction of flutter derivatives by artificial neural networks", *J. Wind Eng. Ind. Aerod*., **96**, 1925-1937.

Chen, X., Matsumoto, M. and Kareem, A. (2000), "Time domain flutter and buffeting response analysis of bridges", *J. Eng. Mech. - ASCE*, **126**(1), 7-16.

Chen, X. and Kareem, A. (2002), "Advances in modeling of aerodynamic forces on bridge decks", *J. Eng. Mech.- ASCE*, **128**(11), 1193-1205.

Chen, X. and Kareem, A. (2008), "Identification of critical structural modes and flutter derivatives for predicting coupled bridge flutter", *J. Wind Eng. Ind. Aerod*., **96**, 1856-1870.

Ding, Q., Zhou, Z., Zhu, L. and Xiang, H. (2010), "Identification of flutter drivatives of bridge decks with free vibration technique", J. *Wind Eng. Ind. Aerod*., **98**, 911-918.

Gan Chowdhury, A. and Sarkar, P.P. (2003), "A new technique for identification of eighteen flutter derivatives using a three-degree-of-freedom section model", *Eng. Struct*., **25**(14), 1763-1772.

Gan Chowdhury, A. (2004), *Identification of Frequency domain and time domain aeroelastic parameters for flutter analysis of flexible structures*, PhD dissertation. Ames (IA), Iowa State University.
Gan Chowdhury, A. and Sarkar, P.P. (2004), "Identification of eighteen flutter derivatives of an airfoil and a bridge deck", *Wind Struct*., **7**(3), 187-202.
Gan Chowdhury, A. and Sarkar, P.P. (2005), "Experimental identification of rational function coefficients for time-domain flutter analysis", *Eng. Struct*., **27**(9), 1349-1364.
Haan, F.L. (2000), *The effects of turbulence on the aerodynamics of long-span bridges*, Ph.D. dissertation. Notre Dame (IN, USA), University of Notre Dame.
Karpel, M. (1982), "Design for active flutter suppression and gust alleviation using state-space aeroelastic modeling", *J. Aircraft*, **19**(3), 221-227.
Lin, Y.K. and Ariaratnam, S.T. (1980), "Stability of bridge motion in turbulent winds", *J. Struct. Mech*., **8**(1), 1-15.
Matsumoto, M. (1996), "Aerodynamic damping of prisms", *J. Wind Eng. Ind. Aerod*., **59**(2-3),159-175.
Roger, K. (1977*), Airplane math modeling methods for active control design*, AGARD-CP-228.
Sarkar, P.P., Gan Chowdhury, A. and Gardner, T.B. (2004), "A novel elastic suspension system for wind tunnel section model studies", *J. Wind Eng. Ind. Aerod*., **92**, 23-40.
Sarkar, P.P., Caracoglia, L., Haan Jr., F.L., Sato, H. and Murakoshi, J. (2009), "Comparative and sensitivity study of flutter derivatives of selected bridge deck sections, Part1: Analysis of inter-laboratory experimental data", *Eng. Struct*., *31*(1), 158-169.
Scanlan, R.H. and Tomko, J.J. (1971), "Airfoil and bridge deckflutter derivatives", *J. Eng. Mech. Div*., **97**(6),1717-1733.
Scanlan, R.H. (1993), "Problematics in formulation of wind-force models for bridge decks", *J. Eng. Mech*.-*ASCE*, **119**(7), 1353-1375.
Zhang, Z., Chen, Z., Cai, Y. and Ge, Y. (2011), "Indicial functions for bridge aeroelastic forces and time-domain flutter analysis", *J. Bridge Eng*.- *ASCE*, **16**(4), 546-557.

CC

Appendix A Definition of matrices and vectors used in the algorithm

$$\underline{C_{h1}} = \begin{bmatrix} \frac{1}{2}\rho\left(U_1\right)^3 & 0 & -\frac{1}{2}\rho U_1 B^2\left(\omega_h\right)^2 & -U_1\frac{L_{h0}^1}{h_0}\cos\phi_{Lh}^1 \\ 0 & \frac{1}{2}\rho\left(U_1\right)^2 B\omega_h & 0 & U_1\frac{L_{h0}^1}{h_0}\sin\phi_{Lh}^1 \\ \frac{1}{2}\rho\left(U_2\right)^3 & 0 & -\frac{1}{2}\rho U_2 B^2\left(\omega_h\right)^2 & -U_2\frac{L_{h0}^2}{h_0}\cos\phi_{Lh}^2 \\ 0 & \frac{1}{2}\rho\left(U_2\right)^2 B\omega_h & 0 & U_2\frac{L_{h0}^2}{h_0}\sin\phi_{Lh}^2 \\ \frac{1}{2}\rho\left(U_3\right)^3 & 0 & -\frac{1}{2}\rho U_3 B^2\left(\omega_h\right)^2 & -U_3\frac{L_{h0}^3}{h_0}\cos\phi_{Lh}^3 \\ 0 & \frac{1}{2}\rho\left(U_3\right)^2 B\omega_h & 0 & U_3\frac{L_{h0}^3}{h_0}\sin\phi_{Lh}^3 \end{bmatrix} \tag{A.1}$$

$$\underline{D_{h1}} = \omega_h\frac{B}{h_0}\begin{bmatrix} L_{h0}^1\sin\phi_{Lh}^1 \\ L_{h0}^1\cos\phi_{Lh}^1 \\ L_{h0}^2\sin\phi_{Lh}^2 \\ L_{h0}^2\cos\phi_{Lh}^2 \\ L_{h0}^3\sin\phi_{Lh}^3 \\ L_{h0}^3\cos\phi_{Lh}^3 \end{bmatrix} \tag{A.2}$$

$$\underline{X_{h1}} = \begin{bmatrix} \left(\underline{\psi_1}\right)_1 \\ \left(\underline{\psi_2}\right)_1 \\ \left(\underline{\psi_3}\right)_1 \\ \lambda \end{bmatrix} = \begin{bmatrix} \lambda\left(\underline{A_0}\right)_{11} \\ \left(\underline{A_0}\right)_{11} + \lambda\left(\underline{A_1}\right)_{11} + \underline{F}_{11} \\ \left(\underline{A_1}\right)_{11} \\ \lambda \end{bmatrix} \tag{A.3}$$

$$\underline{C_{h2}} = \begin{bmatrix} \frac{1}{2}\rho\left(U_1\right)^3 B & 0 & -\frac{1}{2}\rho U_1 B^3\left(\omega_h\right)^2 & -U_1\frac{M_{h0}^1}{h_0}\cos\phi_{Mh}^1 \\ 0 & \frac{1}{2}\rho\left(U_1\right)^2 B^2\omega_h & 0 & U_1\frac{M_{h0}^1}{h_0}\sin\phi_{Mh}^1 \\ \frac{1}{2}\rho\left(U_2\right)^3 B & 0 & -\frac{1}{2}\rho U_2 B^3\left(\omega_h\right)^2 & -U_2\frac{M_{h0}^2}{h_0}\cos\phi_{Mh}^2 \\ 0 & \frac{1}{2}\rho\left(U_2\right)^2 B^2\omega_h & 0 & U_2\frac{M_{h0}^2}{h_0}\sin\phi_{Mh}^2 \\ \frac{1}{2}\rho\left(U_3\right)^3 B & 0 & -\frac{1}{2}\rho U_3 B^3\left(\omega_h\right)^2 & -U_3\frac{M_{h0}^3}{h_0}\cos\phi_{Mh}^3 \\ 0 & \frac{1}{2}\rho\left(U_3\right)^2 B^2\omega_h & 0 & U_3\frac{M_{h0}^3}{h_0}\sin\phi_{Mh}^3 \end{bmatrix} \tag{A.4}$$

$$\underline{D_{h2}} = \omega_h\frac{B}{h_0}\begin{bmatrix} M_{h0}^1\sin\phi_{Mh}^1 \\ M_{h0}^1\cos\phi_{Mh}^1 \\ M_{h0}^2\sin\phi_{Mh}^2 \\ M_{h0}^2\cos\phi_{Mh}^2 \\ M_{h0}^3\sin\phi_{Mh}^3 \\ M_{h0}^3\cos\phi_{Mh}^3 \end{bmatrix} \tag{A.5}$$

$$\underline{X_{h2}} = \begin{bmatrix} \left(\underline{\psi_4}\right)_1 \\ \left(\underline{\psi_5}\right)_1 \\ \left(\underline{\psi_6}\right)_1 \\ \lambda \end{bmatrix} = \begin{bmatrix} \lambda\left(\underline{A_0}\right)_{21} \\ \left(\underline{A_0}\right)_{21} + \lambda\left(\underline{A_1}\right)_{21} + \underline{F}_{21} \\ \left(\underline{A_1}\right)_{21} \\ \lambda \end{bmatrix} \tag{A.6}$$